Magnetic-field enhanced coherence in Ytterbium-doped ring resonators at millikelvin temperatures

THESIS

submitted in partial fulfillment of the
requirements for the degree of

BACHELOR OF SCIENCE
in
PHYSICS

Author :	David van Driel
Student ID :	1328522
Supervisor :	Dirk Bouwmeester, Dapeng Ding
2^{nd} corrector :	Wolfgang Löffler

Leiden, The Netherlands, June 28, 2016

Magnetic-field enhanced coherence in Ytterbium-doped ring resonators at millikelvin temperatures

David van Driel

Huygens-Kamerlingh Onnes Laboratory, Leiden University
P.O. Box 9500, 2300 RA Leiden, The Netherlands

June 28, 2016

Abstract

We measured the homogeneous linewidth Γ_h of ytterbium atoms inside a whispering gallery mode ring resonator. Using two-pulse photon echoes, we looked at the temperature dependence of Γ_h for an applied external magnetic field of $B = 0$ and $B = 0.3$ T. We found a clear narrowing of the linewidth at each temperature. Furthermore, we found saturation of Γ_h for $T < 30$ mK for both $B = 0$ and $B = 0.3$ T. At $T = 10$ mK and $B = 0.3$ T, we have observed a linewidth of 22 kHz, which is very near the lifetime limit of 1 kHz. Our results for the homogeneous linewidth of ions in glasses show that current theories have to be reconsidered. In addition, our results for T_2 ensure that rare earth element-doped cavities are a candidate for AFC quantum memory.

Keywords: Ytterbium, Cavity Quantum Dynamics, Quantum Memory, Tunneling Systems

Contents

Chapter 1

Background

Rare earth elements are 17 elements in the periodic table which were bundled because of their similar chemical properties. A lot of them can be used, for example, for laser gain media. rare earth elements in optical structures have been studied intensely since in the 1980's. They were mainly researched for the possibilities they offer to telecommunications when doped into optical fibers. One such element is ytterbium, which is also a lanthanide, and thus, a metal. Nowadays, rare earth elements are a candidate for quantum memory. This is a system in which light and matter interact, in which data can be stored reliably to be used with quantum computers Predojevic2015. When one dopes a crystal with rare earth elements, individual atoms can be seen in the absorption spectrum. One can potentially address them individually with a narrow linewidth laser. Ytterbium is a good candidate for quantum memory, but the long lifetime of its states makes it hard to study. If ytterbium is embedded in an amorphous SiO_2 host, however, the optical signature of a single Yb ion has never been observed due to reduced coherence. Our particular endeavour involves an ensemble of ytterbium ions in a whispering gallery mode cavity. The cavity is used to enhance the rate of spontaneous emission of the ytterbium ions, and to enhance light-ion interaction. We measure at low temperatures with an external magnetic field to see whether we can reach lifetime-limited coherence.

1.1 Atomic Physics of Ytterbium

Atomic physics allows one to make statements regarding the electronic states of an atom. The Aufbau principle, for example, predicts how electronic shells are filled. Interestingly, they are not filled according to the principle quantum number n, but they are filled in a different manner, depicted in figure 1.1. Values of the azimuthal quantum number l are written as letters here. The table below shows the correspondence.

s	p	d	f	g
0	1	2	3	4

For reference, the set of all allowed states with the same principal quantum number n is called a shell, and all allowed states with the same principal quantum number as well as azimuthal quantum number l a subshell. So $n = 2$ is a shell, $n = 2$, $l = p$ is a subshell.

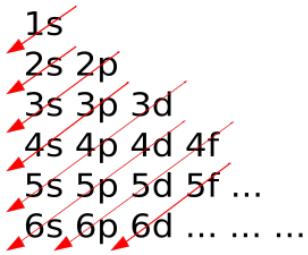

Figure 1.1: *The arrows indicate the filling of states.*

Here, states in the next shell are often filled before filling the previous shell. For example, the 4s subshell is filled before the 3d subshell. This is the case, because the states in the 3d subshell have higher energy than the states in the 4s subshell.

By distributing all 70 electrons of ytterbium, the electronic configuration ultimately reached is the following:

$$[Yb] = 1s^2 2s^2 2p^6 3s^2 3p^6 3d^{10} 4s^2 4p^6 4d^{10} 4f^{14} 5s^2 5p^6 6s^2 = [Xe] 4f^{14} 6s^2 \quad (1.1)$$

This notation means that ytterbium has the same electronic configuration as xenon, with an additional 14 electrons in the 4f shell and 2 electrons in the 6s shell.

The ytterbium atom in our sample is implanted in the glass of the whispering gallery mode cavity. As a result, ytterbium is ionised and loses electrons. This means that we are dealing with Yb^{3+}, the triply ionised version, which has the following electronic configuration: $[Yb^{3+}] = [Xe]4f^{13}$. The f-shell is 7-fold degenerate, and can hold 14 electrons due to spin. For the ionised form of Ytterbium, 13 out of 14 states are filled. This is shown in figure 1.2.

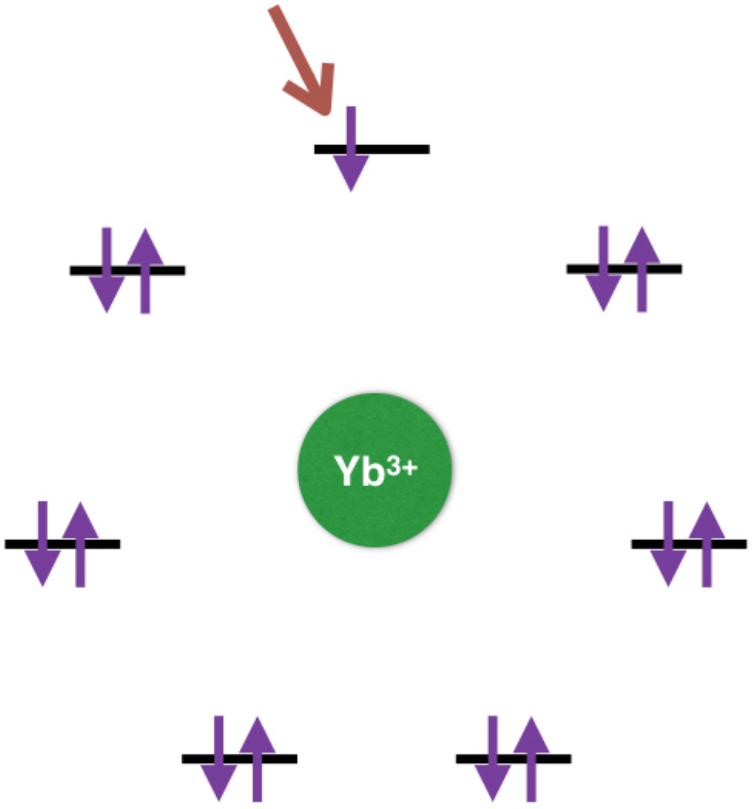

Figure 1.2: *The filling of the 4f subshell of ytterbium. The red arrow refers to the unpaired electron.*

So Yb^{3+} has a spin $s = 1/2$. Additionally, the 4f states have an azimuthal quantum number of $l = 3$. Because of LS coupling, the only good quantum number is j. The total angular momentum quantum number j is equal to $j = |l \pm s|$. Using Russell-Saunders notation [24], we can write down two possible states in the form: ${}^{2s+1}L_j$. These are shown in figure 1.3.

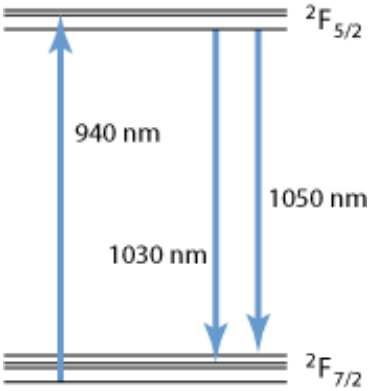

Figure 1.3: *The splitting of levels of Ytterbium as a result of fine structure [18]. Our transition wavelengths are slightly different.*

The fact that our ytterbium atoms are implanted into a cavity changes the level scheme. The ytterbium atoms are placed in the SiO_2 of the cavity. The SiO_2 lattice exerts an electric field on all atoms inside it. This so-called crystal field causes a Stark effect in the ytterbium atoms. The Stark effect not only shifts the energy levels, it lifts the degeneracy of the $^2F_{5/2}$ and $^2F_{7/2}$ states as well. To count these additional states, we now use the index k to describe them. The splitting goes according to: $k = \{1, 2, 3, \ldots, \frac{2j+1}{2}\}$ [9]. Resulting in $k = \{1, 2, 3\}$ for the upper level and $k = \{1, 2, 3, 4\}$ for the lower level. Figure 1.3 shows that $^2F_{5/2}$ is split into 3 states and $^2F_{7/2}$ is split into 4 states. The transitions that we observe, are the ones between these two groups of states. These transitions are electric dipole forbidden, because they are all in the F-shell. This means that they do not satisfy the selection rule: $\Delta L = \pm 1$. This change in L has to occur for the transition dipole moment to be nonzero. In other words: $\langle \Psi_1 | \mu | \Psi_2 \rangle$ will be zero unless Ψ_1 and Ψ_2 have different values of L, because the integral will otherwise be over an odd integrand. Here, Ψ_1, Ψ_2 can denote any two electronic states, in this case $^2F_{5/2}$ and $^2F_{7/2}$. μ is the dipole moment. If a transition is dipole forbidden, it does still occur though, albeit rarely. These transitions are electric dipole forbidden, but meanwhile, they are magnetic dipole and electric quadropole allowed. In addition, the crystal field mixes 4f states with higher, excited states [9]. In doing so, transitions between these mixed states makes them selection rule allowed again. Still, the transitions have a fairly weak oscillator strength.

The splitting due to the Stark effect is on the order of 100 cm^{-1}. The exact splitting differs a lot per host material. Various measurements have been made for ytterbium in different hosts [7, 8, 10, 32]. The exact composition of the glass has a large influence on the size of the splittings. A rough estimate made from these results is depicted in the table below:

ytterbium level ($^{2s+1}L_j^k$)	Energy (cm^{-1})
$^2F_{5/2}^3$	11630
$^2F_{5/2}^2$	10900
$^2F_{5/2}^1$	10200
$^2F_{7/2}^4$	1000
$^2F_{7/2}^3$	600
$^2F_{7/2}^2$	400
$^2F_{7/2}^1$	0

The 4f states in ytterbium have some truly interesting properties. The radial distance of 4f wavefunctions is less than that of 5s and 5p wavefunctions. This means that the 4f states are shielded by the 5s and 5p orbitals. As a result, external perturbations affect the 4f states far less than they would without the presence of the 5s and 5p orbitals [25]. This gives 4f states significant quantum coherence. Correspondingly, the coherence times of such states are very long. For europium in crystalline cavities, coherence times of 4f states up to 6 hours have already been observed [33]. The mentioned 4f, 5s and 5p wavefunctions are shown in figures 1.4 and 1.5.

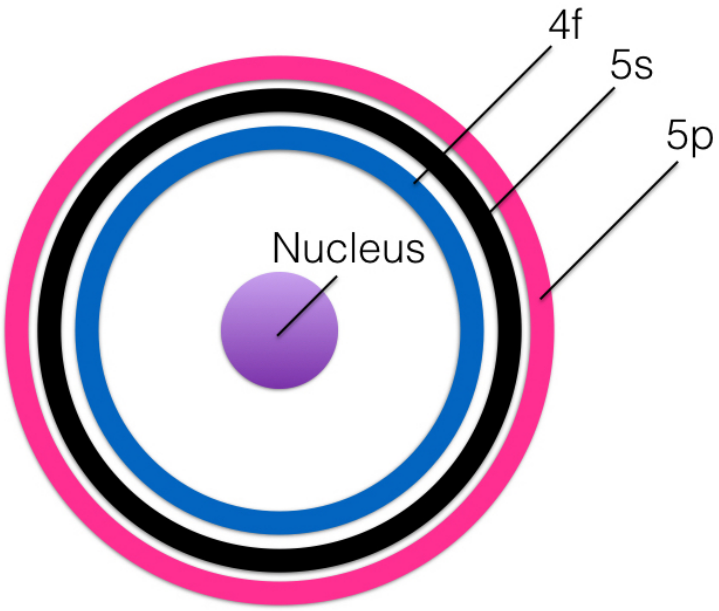

Figure 1.4: *The three outer shells of Yb^{3+} according to the Bohr model. The 4f shell is shielded by the 5s and 5p shells.*

Figure 1.5 depicts the probability distribution of the radial part of the wavefunction. These are Hartree-Fock wavefunctions.

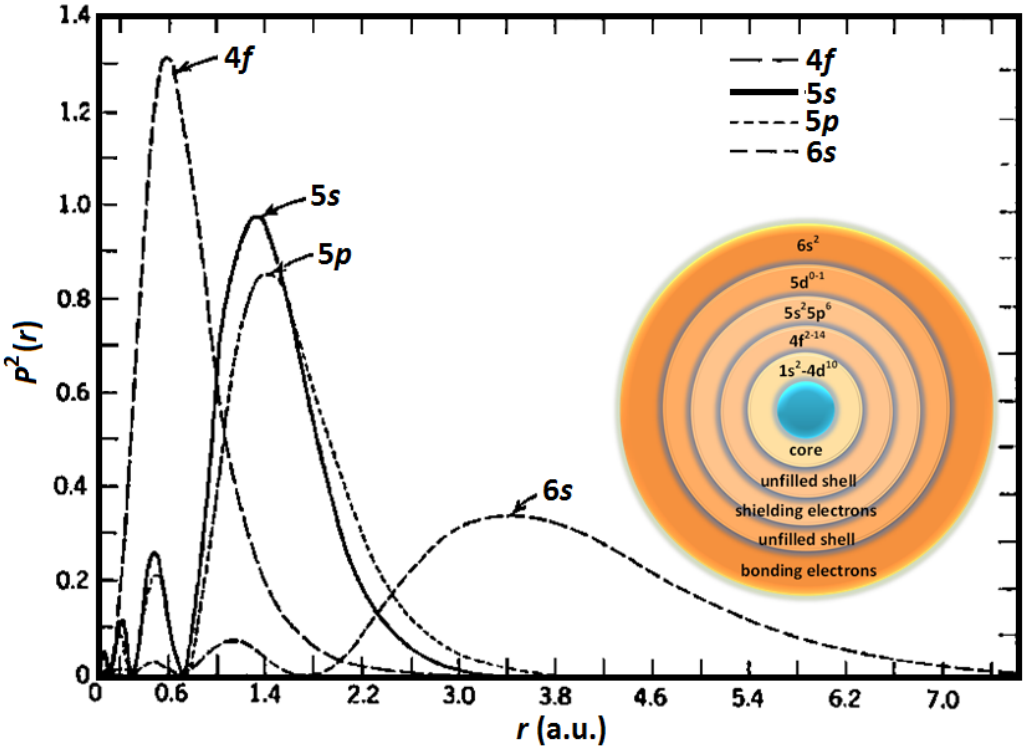

Figure 1.5: *The radial dependence of the probability distribution of the mentioned states [23].*

By applying a magnetic field to the sample, one achieves even further level splitting, as a result of the Zeeman effect. This amounts to each crystal field level being split into two. The resulting level scheme of ytterbium affected by the Zeeman effect is displayed in 1.6. We use equation 1.2 to estimate the size of the Zeeman splitting. The results of which lead to an energy difference per state numbered by m_j of:

$$\Delta E = g_j \cdot B \cdot \mu_B \cdot m_j \tag{1.2}$$

We use a magnetic field with a magnitude of approximately $B = 0.3$ T. Furthermore, we assume $g = 2$. This leads to an energy difference between each subsequent Zeeman level of 8.38 GHz or equivalently, 0.28 cm^{-1}. Of course, the exact splitting differs also between $^2F_{5/2}$ and $^2F_{7/2}$. They have different g-factors that are hard to estimate because the ytterbium is not in vacuum. This means that the Stark and Zeeman splitting differ 4 orders of magnitude. This can be explained by the fact that the crystal field causing the Stark effect is much bigger than the magnetic field causing the Zeeman levels.

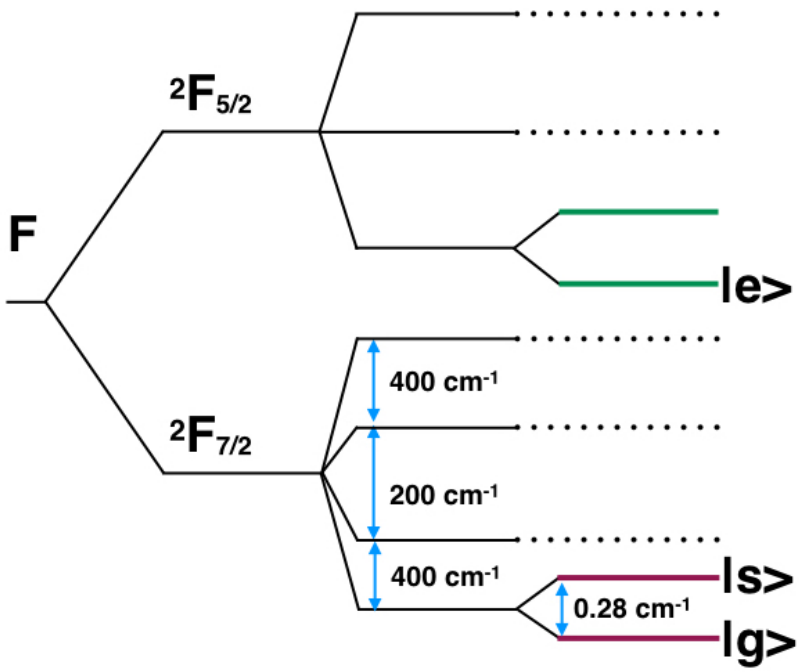

Figure 1.6: *All splittings of Yb^{3+} in our cavity, with an external magnetic field of $B = 0.3$ T.*

Figure 1.6 is a sketch of the level splitting of ytterbium. The absolute size of the splitting is not shown in proportion. When looking at the size

of the Stark splittings as compared to the size of Zeeman splittings, the diagram would look fully different.
4f States have very long coherence times (due to the shielding), and the coherence time for the two Zeeman levels of the ground state can be especially long. Rare earth elements in cavities are suitable for a quantum memory, because the coherence time of a quantum memory has to be much longer than the time it would take a quantum computer to complete one operation on a qubit [11].
Our sample is candidate for an Atomic Frequency Comb (AFC) spin-wave memory [12]. The large inhomogeneous linewidth of the ytterbium atoms in the cavity is especially useful for such a system. This is explained in figure 1.9. Because the yttebrium can be addressed at multiple frequencies, one can make a multimode quantum memory system. To do so, it requires some additional preparation. Namely, the creation of an AFC. Certain ytterbium ions are optically pumped to an auxiliary state. By doing so, the spectrum will look like figure 1.7.

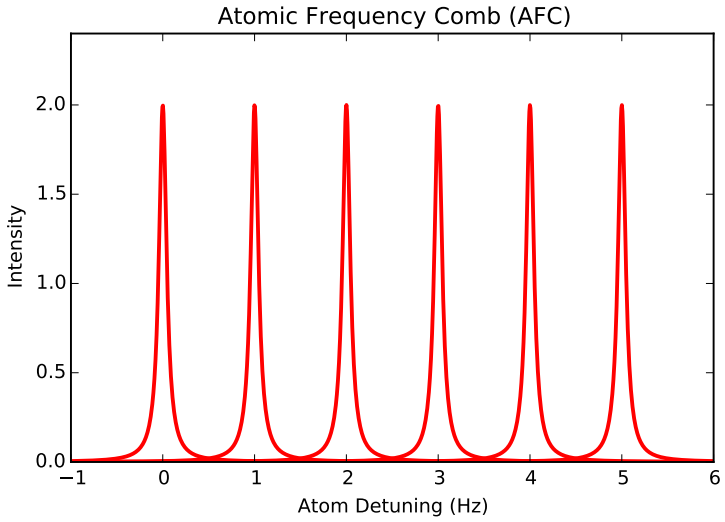

Figure 1.7: *An example of an AFC spectrum.*

Now, atoms are periodically spaced with respect to each other in the frequency spectrum. These peaks represent the intensity of the 4f-4f transitions of ytterbium ions. The x-axis represents atom detuning in terms of frequency with regard to ω_0. When storing information into this quantum memory, a photon is sent in containing all the frequencies in the AFC. Even if only a single photon is sent in, all ytterbium atoms within the bandwidth of the photon are collectively excited. This creates a delocalised, collective

Version of June 28, 2016– Created June 28, 2016 - 15:34

excitation of the ytterbium ions. [1].

After this, a sequence of pulses follows. A simplified overview of how this systems acts as a quantum memory is shown in 1.8.

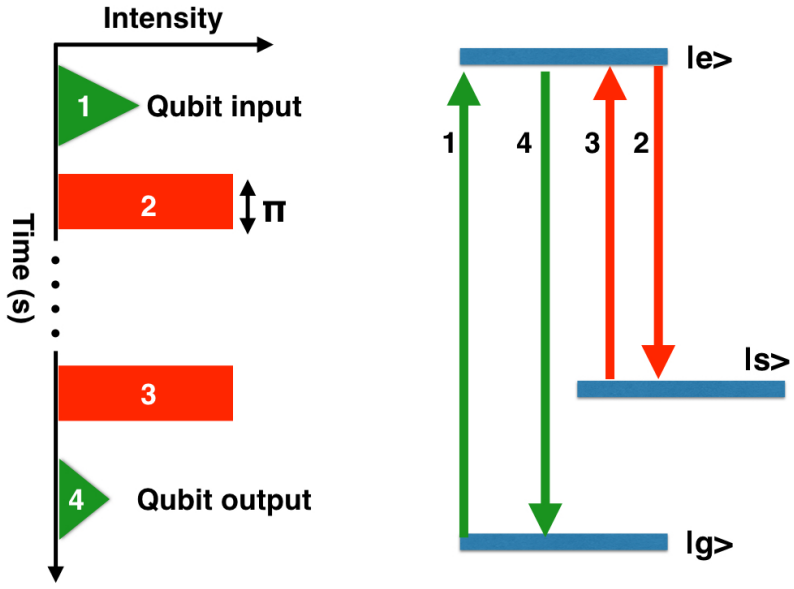

Figure 1.8: *The pulse sequence in AFC quantum memory.*

Here, $|g\rangle$ is the lower Zeeman level of ${}^2F^1_{7/2}$, the lowest crystal level. $|s\rangle$ is the upper Zeeman level of ${}^2F^1_{7/2}$. And $|e\rangle$ is the lower Zeeman level of ${}^2F^1_{5/2}$. The exact positioning of these states is shown in figure 1.6. The memory operates as follows. First, the qubit (a single photon) is absorbed by the material. After a collective delocalized excitation is caused in the material, a control pulse is sent to transfer this excitation to the spin level $|s\rangle$. This is done via a π pulse. In $|s\rangle$, it is stored in the form of a spin-wave. When one wants to retrieve the qubit, pulse number three is sent. This pulse transfers the collective excitation back to the excited state. After some time, $|e\rangle$ goes back to $|g\rangle$ and the photon carrying the information is released.

Version of June 28, 2016– Created June 28, 2016 - 15:34

The question is now whether the homogeneous linewidth of Yb^{3+} is small enough to allow the Yb^{3+} ions to be optically addressed individually. When looking at the entire spectrum, inhomogeneous linewidth is also important. Because the Yb^{3+} ions experience a Stark effect, their resonances are not all at the same frequency anymore. Each Yb^{3+} ion feels a slightly different crystal field, changing the energy difference between $^2F_{5/2}$ and $^2F_{7/2}$ states. The inhomogeneous linewidth refers to the FWHM of the envelope containing all the absorption peaks of the Yb^{3+} ions. The difference between homogeneous and inhomogeneous linewidth is shown in figure 1.9. As we shall see later, the homogeneous linewidth of Yb^{3+} de-

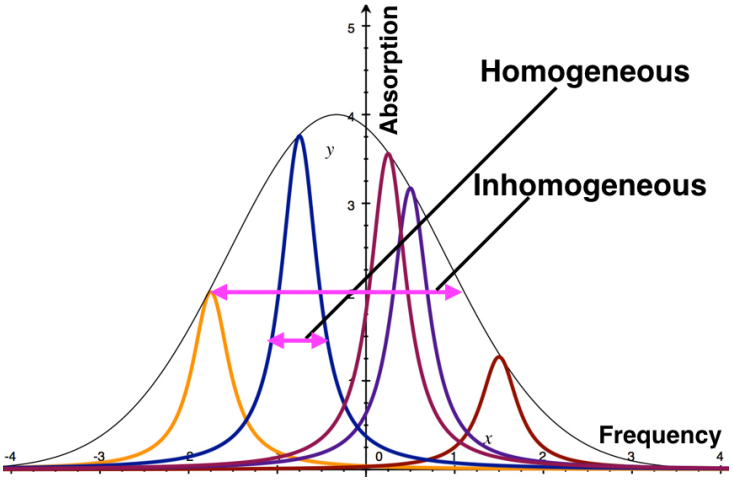

Figure 1.9: *The envelope depicts the inhomogeneous broadening, the widths of the peaks are the homogeneous linewidths of the Yb^{3+} ions.*

creases when they are subjected to a magnetic field. This is due to the increased coherence time of the $^2F_{5/2}$ and $^2F_{7/2}$ states. The relation between coherence time (T_2) and homogeneous linewidth is the following [16]:

$$\Gamma_h = \frac{1}{\pi T_1} + \frac{1}{2\pi T_2^*} = \frac{1}{4\pi T_2} \tag{1.3}$$

Because T_2 increases, Γ_h decreases. We expect the magnetic field to increase the coherence time.

Version of June 28, 2016– Created June 28, 2016 - 15:34

As mentioned earlier, the 4f-4f transitions have a very narrow homogeneous linewidth. They also have a fairly weak oscillator strength. To be able to measure these transitions, the rate of spontaneous emission has to be enlarged. This is the reason the ytterbium is implanted in an optical cavity. Upon placing the ytterbium in a cavity, the rate of spontaneous emission is increased. This is the Purcell effect [22]. By doing so, the 4f-4f transitions are observable.

1.2 Whispering Gallery Mode Ring Resonators

An optical ring resonator is an example of an electromagnetic cavity. In such a system, light is guided into a transparant ring. Just like in a Fabry-Pérot cavity, it has resonance frequencies for which constructive interference takes place. These frequencies depend on the optical pathlength of the ring, which is simply: $OPD = 2\pi rn$. With r being the radius of the ring and n being the refractive index of the ring. An integer number of wavelengths have to fit in this pathlength, so the resonance condition is: $2\pi rn = m\lambda_m$. In order to couple light into the ring resonator, waveguides have to be placed next to the ring. The whole system is shown schematically in figure 1.10. Notice that the waveguides are not touching the ring itself.

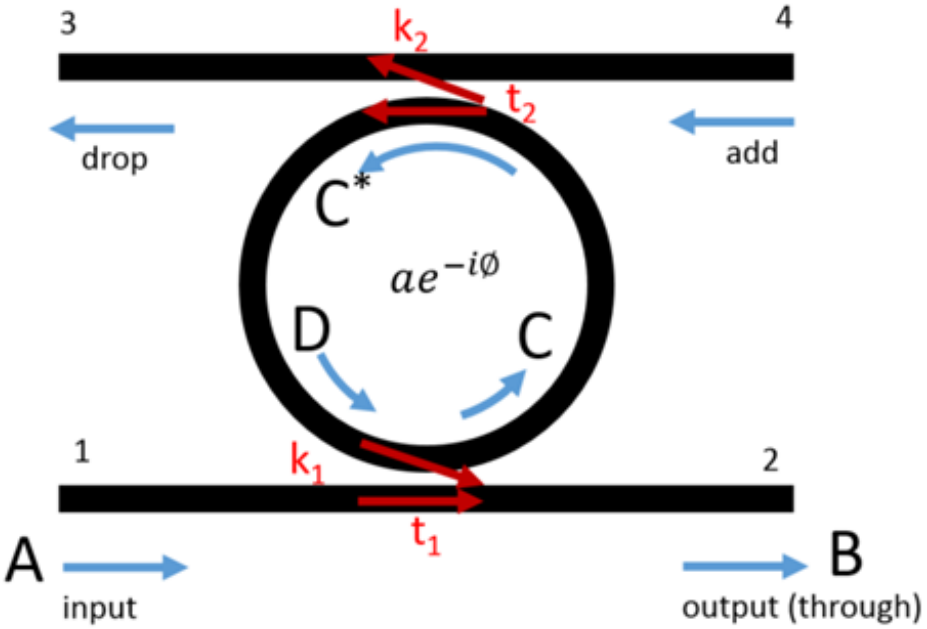

Figure 1.10: *A schematic drawing of a ring resonator [13].*

This ring resonator combined with the two waveguides is a whispering gallery mode ring resonator. Meaning that it uses the principles of total internal reflection and constructive interference to get light into the ring. Eventually, light leaves the cavity, but it can remain inside for a lot of roundtrips. Such cavities can achieve Q-factors of up to 10^9 [26].

Version of June 28, 2016– Created June 28, 2016 - 15:34

In figure 1.11, a whispering gallery mode resonator is depicted. This is not the sample we use to measure coherence times. It does not even contain ytterbium. It is though, a much smaller and improved ring resonator as compared to the one we used.

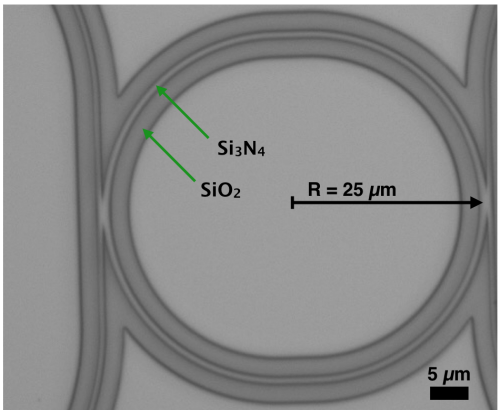

Figure 1.11: *A Whispering Gallery Mode ring resonator.*

In order to see whether this new cavity would enhance our total system, we attempted to measure a cavity mode. This is shown in figure 1.12.

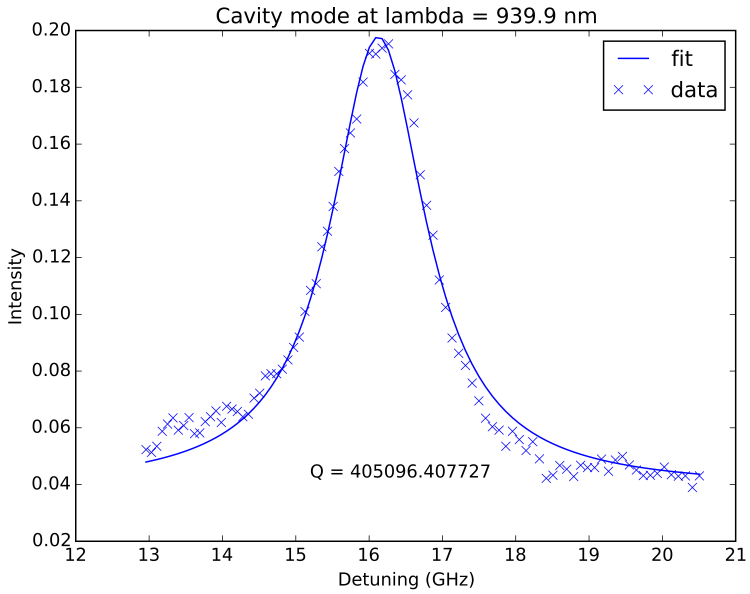

Figure 1.12: *A cavity mode around $\lambda = 939.9$ nm.*

At a detuning of 0 GHz, the frequency would correspond to $\lambda = 939.9$ nm. This cavity has a Q-factor of $Q = 4.0 \cdot 10^5$. To measure this cav-

ity mode, we send in the laser at one of the waveguides. This proces is shown in 1.13. This figure depicts the same ring resonator as shown in

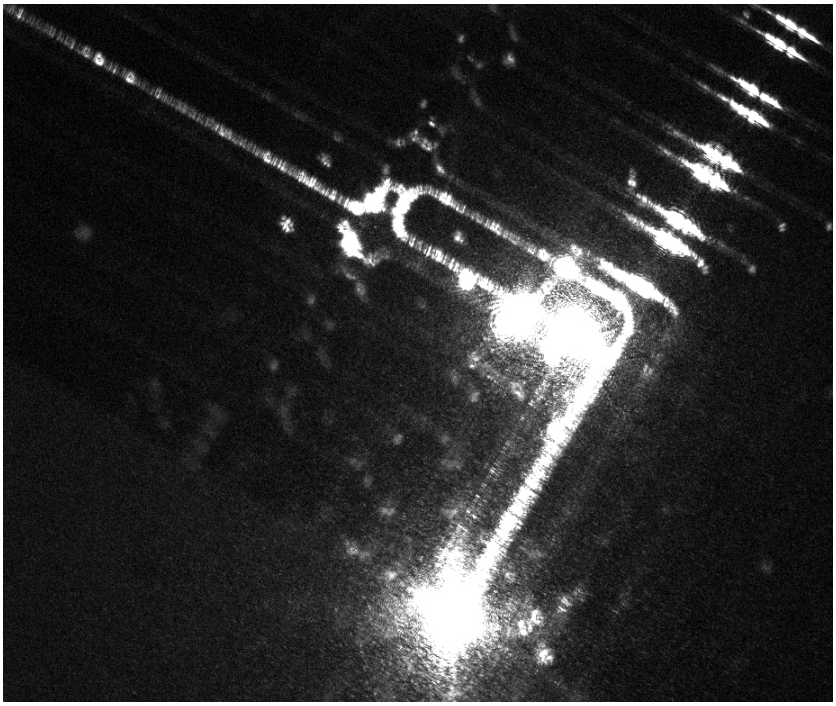

Figure 1.13: *The way light couples into a cavity. Notice parts other waveguides lighting up as well.*

1.11. The light enters one of the waveguides and couples into the ring. On can see one wave guide (and the other faintly) on the other side of the ring light up. Furthermore, some light also couples into the waveguide running back to the input side of the ring resonator. To be able to measure a cavity mode, we sweep the laser in a certain range. Then, we look at the light coming out of one of the waveguides leaving the ring. This light is detected by a femtowatt receiver, which measures the intensity when we vary the frequency. Coupling into a waveguide is very critical, seeing as the distances are very small. The width of the Si_3N_4, for example, is about 800 nm. These samples might prove to be useful in the future, but our coherence time measurements were performed in an ytterbium-doped ring resonator. This ring resonator is shown in 1.14.

1.3 Sample

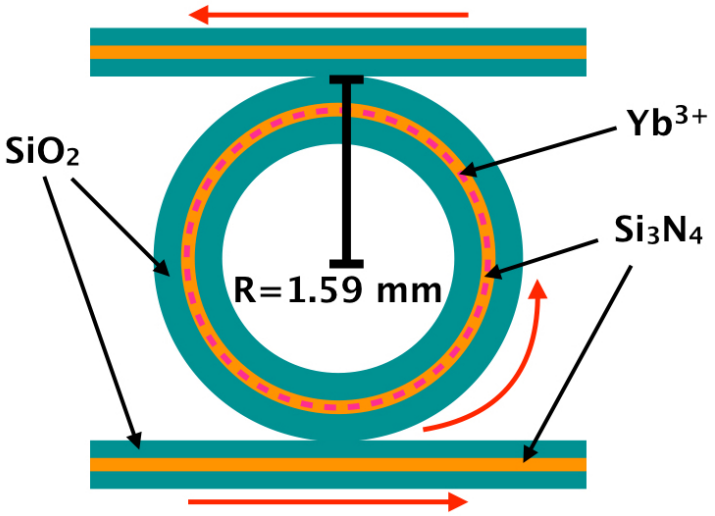

Figure 1.14: *A top view of the ytterbium-doped ring resonator. Red arrows indicate the direction of propagation of the light.*

The rectangles bordering the ring are the waveguides. Light is sent into the Si_3N_4. Due to evanescent interaction, light manages to couple into the Si_3N_4 of the ring resonator. The ytterbium is implanted some distance above the Si_3N_4 layer. The distance between the Yb^{3+} layer and the Si_3N_4 layer is approximately 72 nm. Because of this small distance, the ytterbium can still be excited by the light propagating in the Si_3N_4.

So to summarise, the ring resonator and waveguides consist of these three materials:

1. Very pure, amorphous fused silica: SiO_2.

2. Si_3N_4. This has a higher refractive index than the SiO_2. Due to the difference, light in the waveguides is totally internally reflected.

3. Yb^{3+} ions. These were implanted into the SiO_2 using an ion-gun. The concentration amounts to 0.001 atom percentages. Meaning that 0.001% of all silicon or oxygen atoms is replaced by Yb^{3+}.

A cross-section of the ring is shown in figure 1.15.

The ytterbium atoms are implanted in the SiO_2, following a gaussian

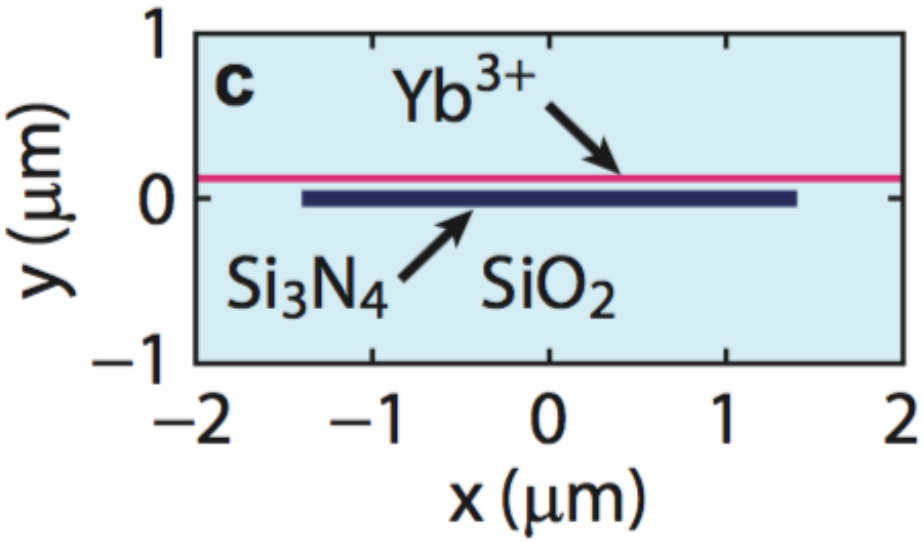

Figure 1.15: *A cross-section of the ring resonator. The ytterbium is placed 72 nm above the Si_3N_4 [4].*

distribution in depth. The peak of the ytterbium distribution lies at 0.001 atom percentages. The depth at which this peak concentration lies is 128 nm. The Yb^{3+} as well as the Si_3N_4 are both fully immersed in the SiO_2.

1.4 Properties of Amorphous Solids

The ytterbium atoms are implanted in SiO_2. The SiO_2, however, is amorphous instead of crystalline. The crystalline variant is referred to as quartz, the amorphous version is known as silica. The difference between the two sorts is shown in 1.16. As a host material for the ytterbium, one could use either one of them. Silica is arguably the best material for a cavity, which is why we use it. The downside of using silica instead of class, is that it decreases the coherence of our ytterbium atoms, due to the presence of so-called tunneling systems. Silica is also hard to model. The amorphous structure makes it difficult to make reliable estimates with regard to its properties. Furthermore, the local differences in amorphous SiO_2 can be very large. Ytterbium in one position in the material might have very different properties than in another spot.

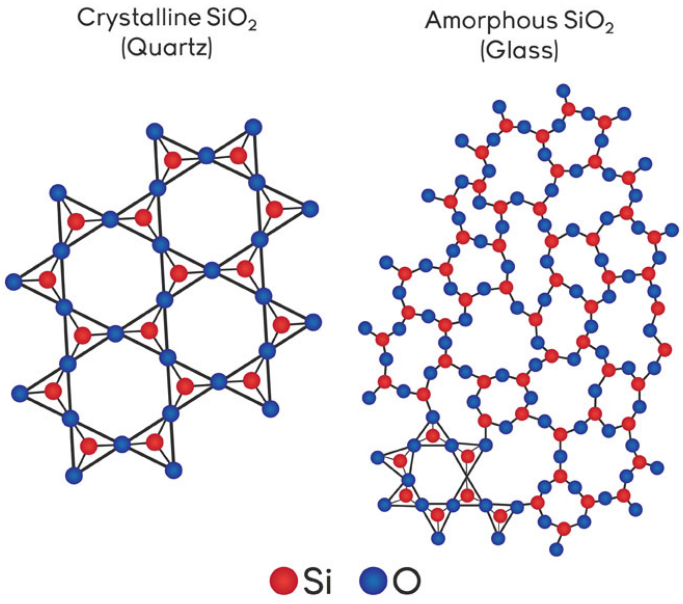

Figure 1.16: *The structural differences between different types of SiO_2 [5].*

Even though the SiO_2 is amorphous, it still has some kind of lattice. Macroscopically, it is a disordered material. Locally, it does have a structured placement of atoms. This local crystalline structure gives rise to an electric field in the silica. This so-called crystal field differs a lot locally, due to the amorphous nature of the silica. The crystal field causes a Stark effect in the ytterbium ions. This is responsible for the level splitting in fig-

ure 1.6. Additionally, the local differences of the crystal field are responsible for slightly different energy levels for each ytterbium atom. The crystal field can also slightly change over time. Perturbation theory explains how the energy reacts:

$$E(t)_i^{(1)} = \langle \Psi_i | \, V(x,y,z,t) \, | \Psi_i \rangle \tag{1.4}$$

Here, $|\Psi_i\rangle$ is a state of ytterbium and V is the crystal field. The energy is time-dependent because the SiO_2 molecules in the glass host move slightly over time. The effect this has on the frequencies of the ytterbium ions is known as spectral diffusion. This process leads to decoherence, giving rise to homogeneous linewidth broadening (see figure 1.9) [17]. Spectral diffusion is especially troublesome for relatively long measurements, like stimulated three-pulse echoes, spectral hole burning and two-pulse echoes. The reason for this is the relatively long timescale of spectral diffusion.
Another mechanism, which leads to decoherence is the existence of tunneling systems. tunneling systems are used to explain the homogeneous linewidth broadening of glasses and crystals at low temperatures. The tunneling systems (TS) were introduced in the 1970's by Philips [19]. Since then, the model has been expanded to account for further phenomena. They are also ascribed properties which allow them to couple to external magnetic fields [15]. Also, coupling of ions in glasses to TS were included [28]. So far, they have proven very useful in explaining decoherence phenomena in amorphous solids. One can interpret these states, as (groups of) silicon and oxygen atoms that tunnel between configurations in the silica. This means that they have to overcome an energy barrier in order to switch between two stable states. This tunneling accounts for decoherence, which -through T_2- causes the homogeneous linewidth broadening. The energy diagram of the tunneling systems is depicted in 1.17.

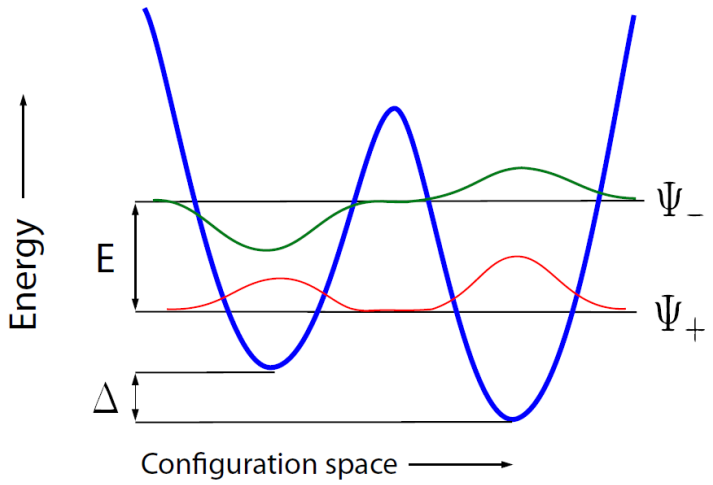

Figure 1.17: *The tunneling occurs because of the energy barrier. Notice the asymmetry between wells [31].*

These TS become relevant at low temperatures. Generally, they should be taken into account for $T \leq 1$ K[19]. We measure at significantly lower temperatures. Namely, between 10 and 80 mK. Here, the linewidth follows a dependence of $\Gamma \propto T^{1.3}$ [6]. Huber states that a dipole-dipole elastic interaction can account for the magnitude and temperature-dependence of the linewidth at these temperatures.
The addition of an external magnetic field even further complicates these phenomena. We expect the magnetic field to narrow the homogeneous linewidth. Staudt et al. have shown that the homogeneous linewidth of rare earth elements in optical fibers decreases exponentially as a function of external magnetic field strength [28]. MacFarlane introduces: "field-dependent elastic tunneling modes that acquire a magnetic character by coupling to the spins" [15]. We have reasons to expect this to happen in our sample as well. Our hypothesis is that the external magnetic field couples to an angular momentum of sorts, found in the TS. In this model, we assign (spin) angular moments to both wells. One potential well having angular momentum *up* and the other having *down*. The energy resulting from the interaction between TS angular momentum and a magnetic field is described by:

$$E = -\vec{B} \cdot \vec{\mu} \tag{1.5}$$

in which μ is the magnetic moment of the well and $\vec{B}$ is the external mag-

netic field. For this set-up, μ can be written as $\vec{\mu} = g\frac{q}{2m}\vec{S}$. With g being the landé factor, m the mass and q the charge. $\vec{B}$ can be written as $\vec{B} = \vec{B_0}cos(\omega t)$. We make the magnetic field time-dependent through of frequency ω. Combining gives the resulting energy:

$$E = g\frac{q}{2m}cos(\omega t)\vec{S}\cdot\vec{B_0} \tag{1.6}$$

Using first-order perturbation theory, one retrieves the perturbation hamiltonian in the basis of the states shown in figure 1.17.

$$H = \frac{1}{2E}\begin{pmatrix} \Delta & \Delta_0 \\ \Delta_0 & -\Delta \end{pmatrix} g\frac{q}{2m}|\underline{B}|cos(\omega t) \tag{1.7}$$

Here, Δ, Δ_0 denote the energy asymmetry (as seen in 1.17) and a tunneling related parameter respectively. More specifically [31]:

$$\Delta_0 = Ae^{-\frac{d\sqrt{2mV}}{2\hbar x}} \tag{1.8}$$

The magnetic field increases the energy difference between the two TS modes. So, via the tunneling parameter, an external magnetic field would theoretically decrease the chance of tunneling.

Chapter 2

Experiments and Results

2.1 Technique

The photon echo technique is a beautiful way to measure the homogeneous linewidth in an inhomogeneously broadened ensemble of Yb^{3+} ions. The $^2F_{5/2}$ and $^2F_{7/2}$ states of ytterbium form a two-level system. Each such two-level system can be imagined to be a point in the Bloch sphere. This Bloch sphere is depicted in figure 2.1.

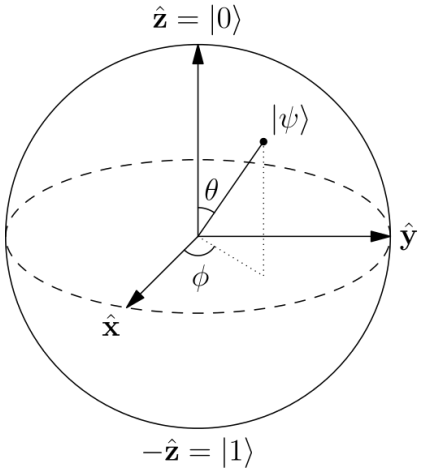

Figure 2.1: *The Bloch sphere allows one to write each two-level-system as a superposition in a sphere [30].*

A Bloch vector is shown in figure 2.1 as $|\Psi\rangle$. The z axis represents the population. So a point on the upper pole means that the entire population is in the excited state, whilst the antipode means that the entire popula-

tion is in the ground state. Our system is not truly a two-level system, since we have another energy level due to the Zeeman splitting, but the Bloch sphere is intuitively very useful. If one sends in a laser with a frequency $\omega_0 = E_0/\bar{h}$ corresponding to the energy difference between $^2F_{5/2}$ and $^2F_{7/2}$, the Bloch vector will start to precess. Because this laser excites the system, the Bloch vector will rotate around the x axis.

An example Bloch vector shown in figure 2.1 is:

$$|\Psi\rangle = cos(\theta/2)\,|0\rangle + e^{i\phi}sin(\theta/2)\,|-1\rangle \tag{2.1}$$

This is a wavefunction on the surface of a unity sphere. The angle θ dictates the mentioned populations and excited and ground states. So upon pumping the system, one changes the angle θ of the Bloch vector.

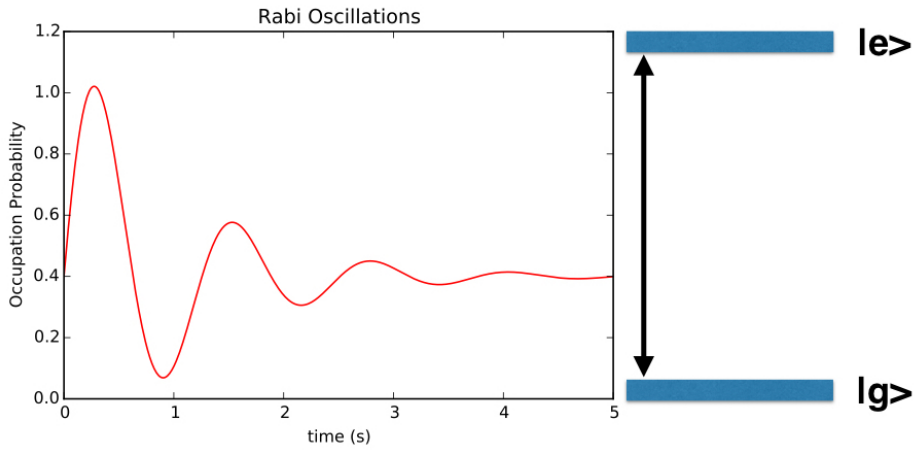

Figure 2.2: *The Rabi oscillations of the ytterbium two-level system.*

By optically pumping the system, one periodically drives the ensemble of ytterbium ions from excited state to ground state. These cycles are called "Rabi oscillations" and are displayed in figure 2.2. The frequency with which the Bloch vector precesses when optically pumping the system is known as the Rabi frequency. Each Yb^{3+} ion has slightly different energy levels, due to the silica they are implanted into. This means that, in the Bloch picture, each ion has a different Rabi Frequency. The Rabi frequency is given by:

$$\Omega = \frac{\vec{d}_{ij} \cdot \vec{E}}{\hbar} \tag{2.2}$$

With $\vec{d}_{ij}$ being the transition dipole moment between initial and final states, and $\vec{E}$ being the electric field incident on the ytterbium ions. If one excites

a population of Ytterbium atoms with a laser, some Bloch vectors will start to precess in the frame rotating with the lasers frequency. This is the photon analog to the excitation of spins in nuclear magnetic resonance. We define the detuning $\delta_i = \omega_i - \omega_0$. With $\omega_i = E_i/\hbar$ being the frequency corresponding to the energy difference between ground and excited states. And ω_0 being the frequency of the laser. For each ion i, this δ_i shows how fast it will dephase with regard to the frequency of the excitation ω_0.
In the Bloch sphere, one can distinguish two characteristic times: T_1 and T_2. T_1 is the population decay time, whilst T_2 is the decoherence time. In NMR, T_1 is also called the longitudinal relaxation time and T_2 is known as the transversal relaxation time. The former is called longitudinal because it determines the rate at which a vector in the Bloch sphere reverts to a thermal equilibrium between excited and ground states. In figure 2.1, this is the equilibrium value for θ. The latter is called transversal because it determines how long it takes the Bloch vector to revert back to a spot on the z axis.
Measuring T_1, T_2 is desirable, seeing as they relate to the homogenous linewidth Γ_h of the emitted light via the relation [16]:

$$\Gamma_h = \frac{1}{\pi T_1} + \frac{1}{2\pi T_2^*} = \frac{1}{4\pi T_2} \tag{2.3}$$

Here, T_2^* is a decoherence time, which originates from pure dephasing effects due to, for example, thermal excitations. Logically speaking, this time is negligible at low temperatures. The aim of this experiment is to find Γ_h at low temperatures when a magnetic field is applied to the sample. To do so, we measure T_2. This is done via a 2PE, a 2-pulse echo. A schematic overview of a 2PE is shown in figure 2.3.

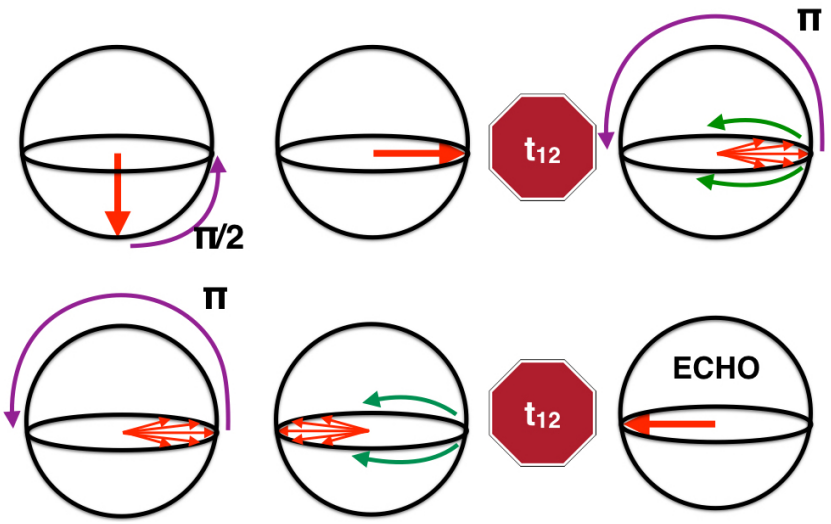

Figure 2.3: *The orientation of the Bloch vectors during a 2PE.*

To be sure, one arrow in figure 2.3 is schematic and actually denotes multiple Bloch vectors overlapping. Due to the variation in the Rabi frequency, the dephasing for each ytterbium ion is different. The first pulse of the 2PE is a $\frac{\pi}{2}$ pulse. This means that $\frac{\pi}{2} = \Omega t$ [27]. So the duration of the laser pulse times the Rabi frequency is equal to $\frac{\pi}{2}$. In our system, the duration of $\frac{\pi}{2}$ pulse is 60 ns. After this pulse ends, the Bloch vectors are in an equal mixture of excited and ground states. In figure 2.3, each Bloch vector in the equator of the Bloch sphere is such an easy mixture. Furthermore, the vectors will start to dephase in accordance with the detuning: $\delta_i = \omega_i - \omega_0$.
After a waiting time t_{12}, the Bloch vectors have all shifted with respect to the vector with $\omega_i = \omega_0$.
Then, a π pulse is sent in. Logically, this is a pulse with the same frequency but twice the duration of the $\frac{\pi}{2}$ pulse. This pulse flips the Bloch vectors 180 $^\circ$ over the x axis.
However, the pulse does not lead to a change in time evolution of the Bloch vectors.
So after the same time t_{12} as after the $\frac{\pi}{2}$ pulse, all the Bloch vectors are aligned again. This leads to the emission of photons, hence the name photon echo. The amount of photons emitted in the echo scales with t_{12}. In fact, by varying this t_{12} and measuring the photons, one can find T_2, via the relation:

$$I \propto e^{-t_{12}/T_2} \tag{2.4}$$

2.2 Experimental Setup

The total setup is depicted schematically in figure 2.4.

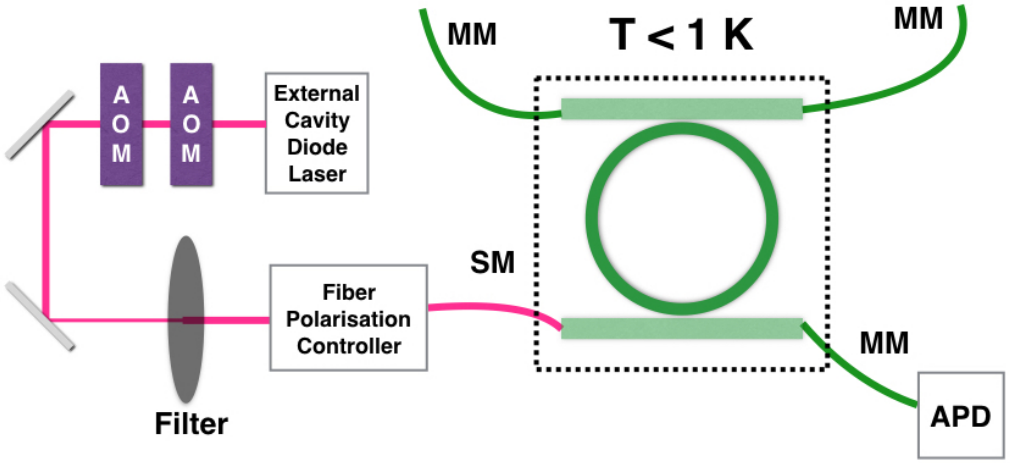

Figure 2.4: *The total setup showing the optical instruments as well as the cryostat.*

Here, AOM indicates the Acousto-Optic Modulator. This apparatus uses acoustic waves to create a grating for the laser. By switching it on and off, one can make a gated laser. We use this to time the $\frac{\pi}{2}$ and π pulses. Even if the AOM is off, the laser can still by refracted up to first order by the crystal. As a result, we use two AOMs to reduce the photon dark count rate.
The filter is used to attenuate the laser power. If the laser power is too high, we just fully excite the whole system, and a 2PE will not work. For the cavity mode we choose, we tune the laser so that the cavity output is at 100 mV. We do this by adding a filter to the setup to reduce the lintensity of the light.
APD is an acronym for Avalanche Photodetector. This detector counts the amount of photons which escape the cavity.
The fibre polarisation controller mechanically presses the fiber, in order to tune the polarisation of the light passing through.
The dotted square in figure 2.4 indicates the cryostat. In here are the waveguides (green rectangles) and the ring resonator (circle). The temperature in this cryostat is below 1 K.
In total, four fibers leave the cryostat. 3 of which (the green ones), are multimode (MM), meaning that they allow multiple modes of electromagnetic waves through. The other fiber -coloured red in the drawing- is single

Version of June 28, 2016– Created June 28, 2016 - 15:34

mode. The glass fibers are coupled to the waveguides with optical glue. First, the fiber and waveguide are covered in this glue. When they have been positioned correctly, the glue is cured with an UV lamp. The glue then hardens and keeps the waveguide and fiber in place. The glue is also transparant for the wavelength of the laser we use. This way, we make sure that the coupling between the fiber and the waveguide is good.
We did measurements with, and without a magnetic field. For the measurements with a magnetic field, we used a NdFeB magnet, with a field of $B = 0.41$ T at millikelvin temperatures. For these measurements, we placed the magnet above the waveguides and the ring resonator.
The experimental setup is shown in figure 2.6.

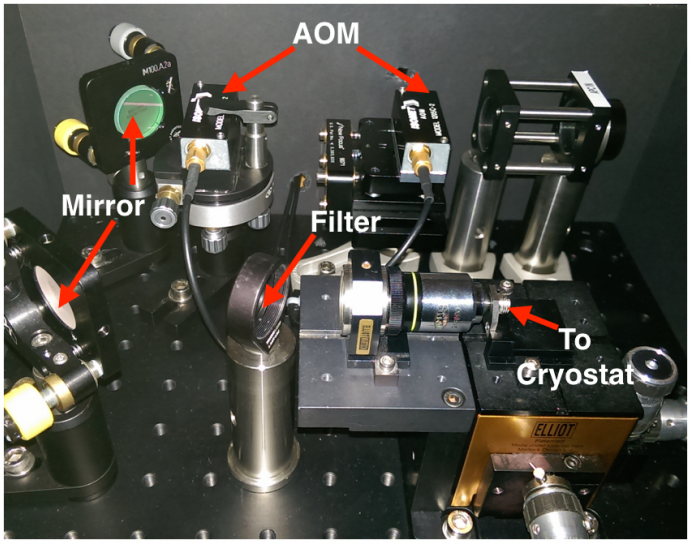

Figure 2.5: *The optical table used in our setup.*

Here, the laser enters into the two AOMs -which are used to accurately pulse the laser- and is carried via a filter into a fiber. The fiber leads the gated laser into the cavity. For the pulses, we use an external cavity diode laser made by toptica. This laser allows us to tune the wavelength slightly. It has a very narrow linewidth ($\propto$ 100 kHz). We manually tune this laser on a cavity mode with a high Q-factor. This cavity mode has a linewidth of about 150 MHz. The inhomogeneously broadened spectrum is quite wide as compared to these two wavelengths. Its linewidth is: 1.57 GHz.

We measure at temperatures down to $T = 10$ mK.To reach these millikelvin temperatures, we use a cryostat with multiple stages. Each subsequent stage reaches a lower temperature. First, it cools using two pulse tubes. Then, it uses the expansion of He-4 to move the heat to other stages. In the last stages, it uses a dillution refrigerator. This dillution refrigerator uses a mixture of He-3 and He-4 to achieve millikelvin temperatures [20].

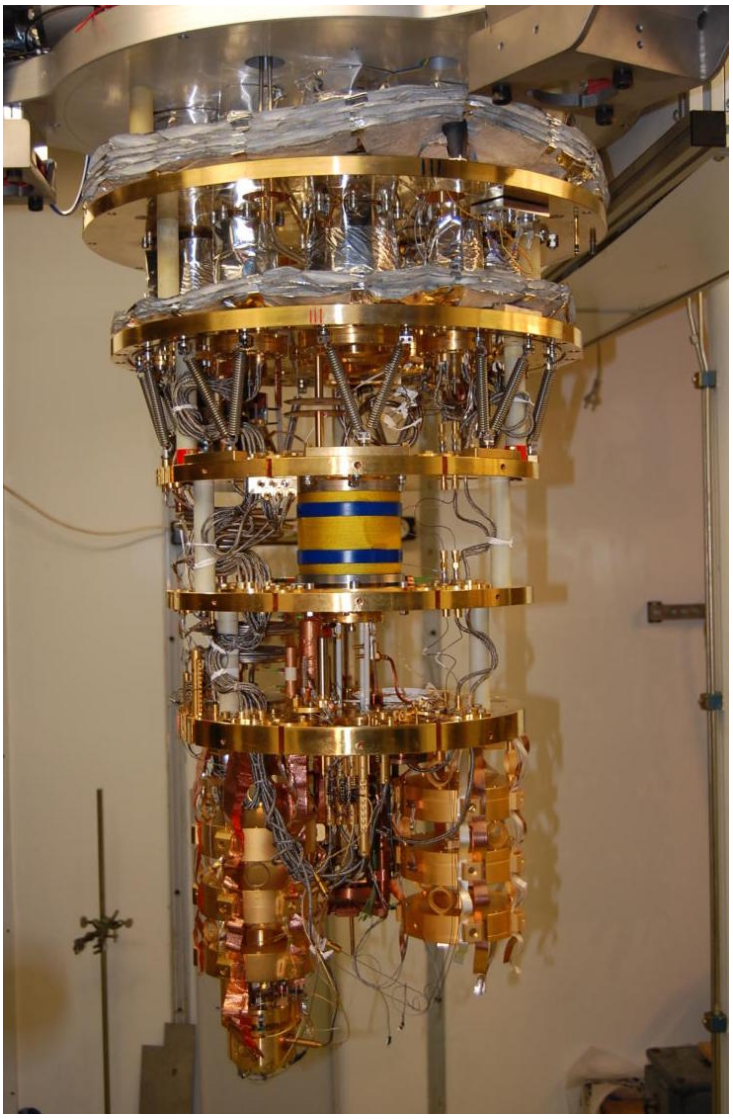

Figure 2.6: *The 'Yeti' cryostat when it is open. Our sample rests on the bottom stage.*

2.3 Results

The core of the measurement is the $\frac{\pi}{2}$ and π pulses followed by an echo. An example of such a measurement is shown in figure 2.7. Here, all signals involved in a 2PE (2 pulse echo) are shown.

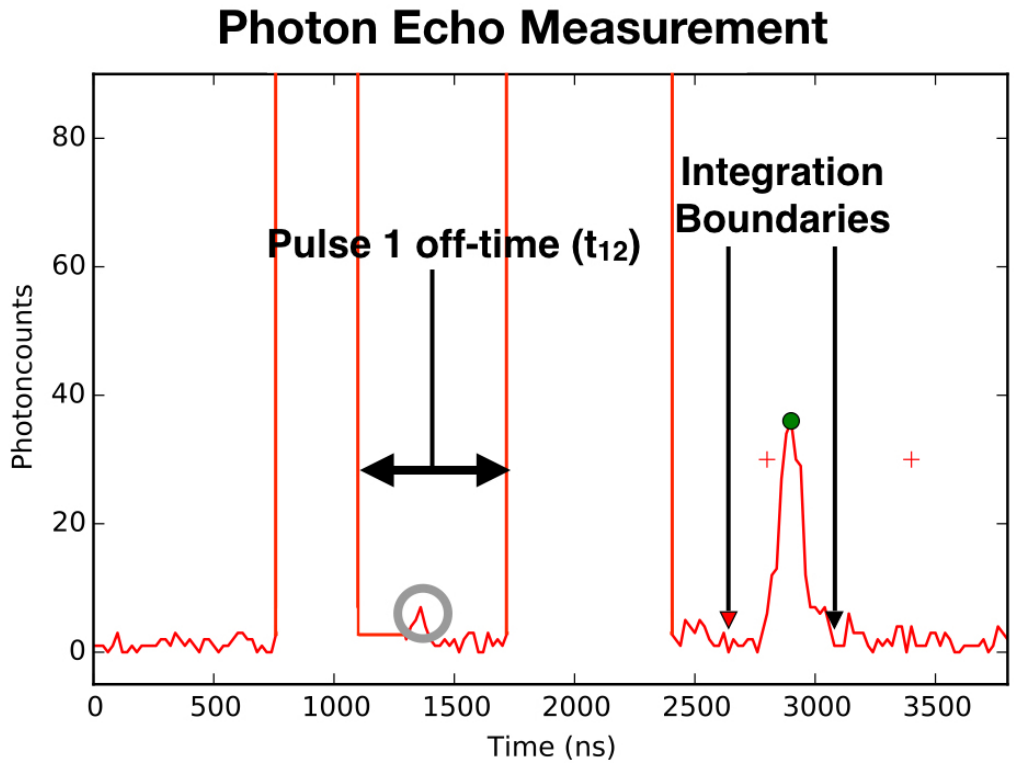

Figure 2.7: *A trace of one 2PE measurement. The $\frac{\pi}{2}$ and π pulses have a much higher intensity than the echo.*

First, a $\frac{\pi}{2}$ pulse is sent into the ring resonator around $t = 800$ ns. Afterwards, the pulse is stopped for a certain off-time. After the off-time, a π pulse is sent. One can see a certain background in the trace. These are the photon dark counts. Photons are not only emitted during the echo, but during the entire the entire 2PE. The gray circle in figure 2.7 shows an additional, smaller peak, as a result of rephasing after the $\frac{\pi}{2}$ pulse. To analyse the trace, we need to determine the area of the photon echo. To do so, we use a program written in iPython notebook. This program will automatically analyse all individual photon echo traces to determine the homogeneous linewidth at a certain temperature. Because we know the duration of the pulses, as well as the off-time, we can estimate where the photon echo peak should be. The red crosses in the trace indicate the win-

dow in which the program will look for a peak. The peak found by the program is illustrated with a green dot. After the peak has been found, the program will roughly determine the boundaries between which it will integrate the photon counts. These are marked with red, respectively, black arrows. All the counts in this window are then summed to form the photon echo intensity. This process is then repeated for a series of off-times. Mostly, these times range from 0.2 to 5.3 μs. Then, we plot all photon echo intensities as a function of this off-time. A result for such a plot is shown figure 2.8

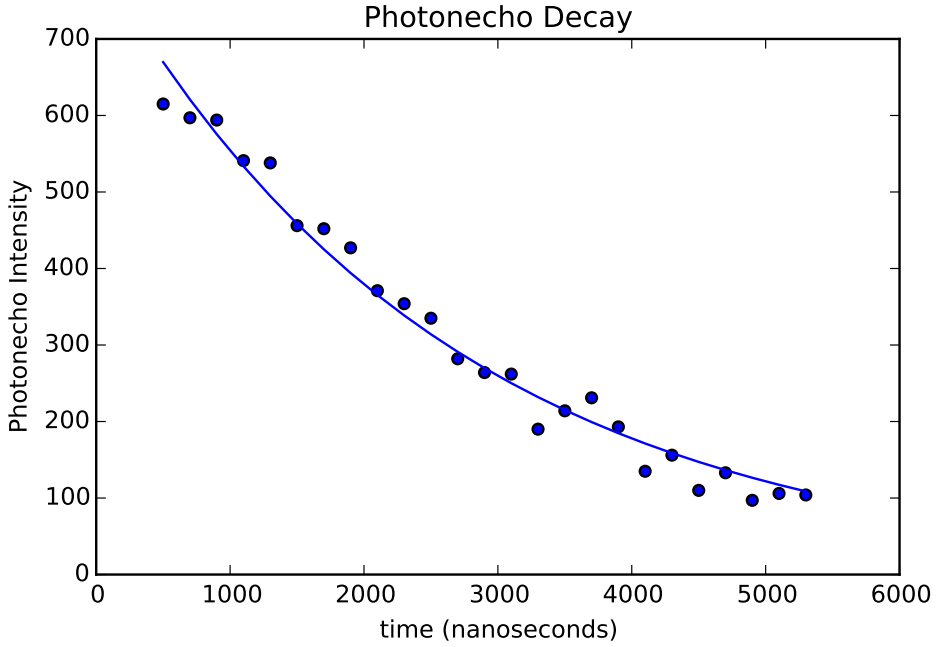

Figure 2.8: *A fit for the photon echo intensity as a function of the off-time at $T = 63$ mK.*

We know that the photon echo intensity falls off like e^{-t_{12}/T_2}. So to find T_2, we perform a least-squares fit with:

$$I = Ae^{-t_{12}/B} \tag{2.5}$$

With A and B being fit parameters. We then use the error on the fit parameter B to estimate the two standard deviations error on T_2. This gives us the coherence time -and correspondingly the homogeneous linewidth- at one temperature. This process is repeated at multiple temperatures to give our final result. This is shown in figure 2.9.

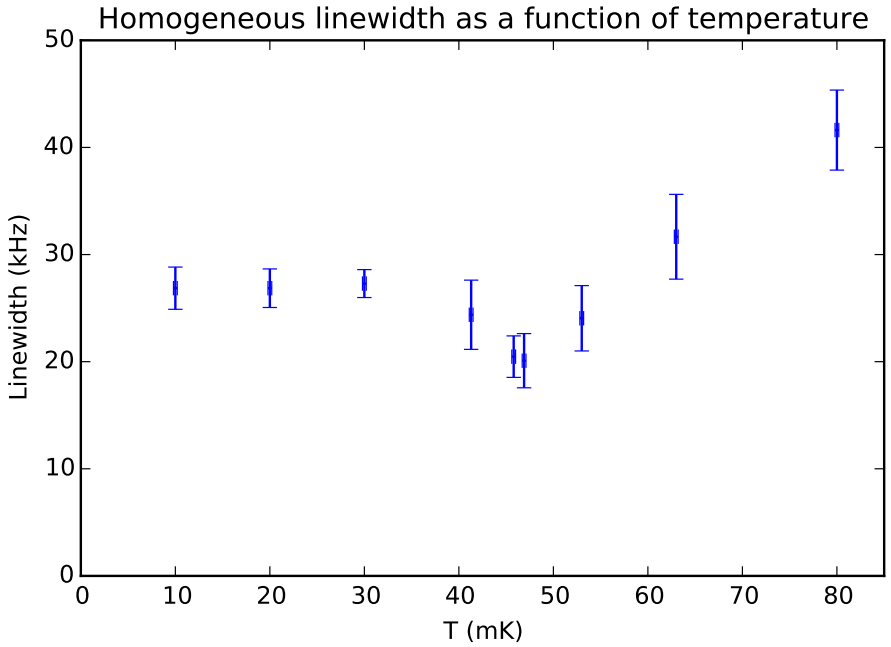

Figure 2.9: *The temperature-dependence of the homogeneous linewidth with* $B = 0.3$ *T.*

In this graph, linewidth is shown as a function of temperature. Interestingly, the linewidth seems to have a local minimum around $T = 46$ mK. The exact nature of this minimum is hard to predict. And unfortunately, the data is too statistically insignificant to be able to definitively call it a minimum. The main question is what the magnetic field does to the homogeneous linewidth. The comparison is shown in figure 2.10.

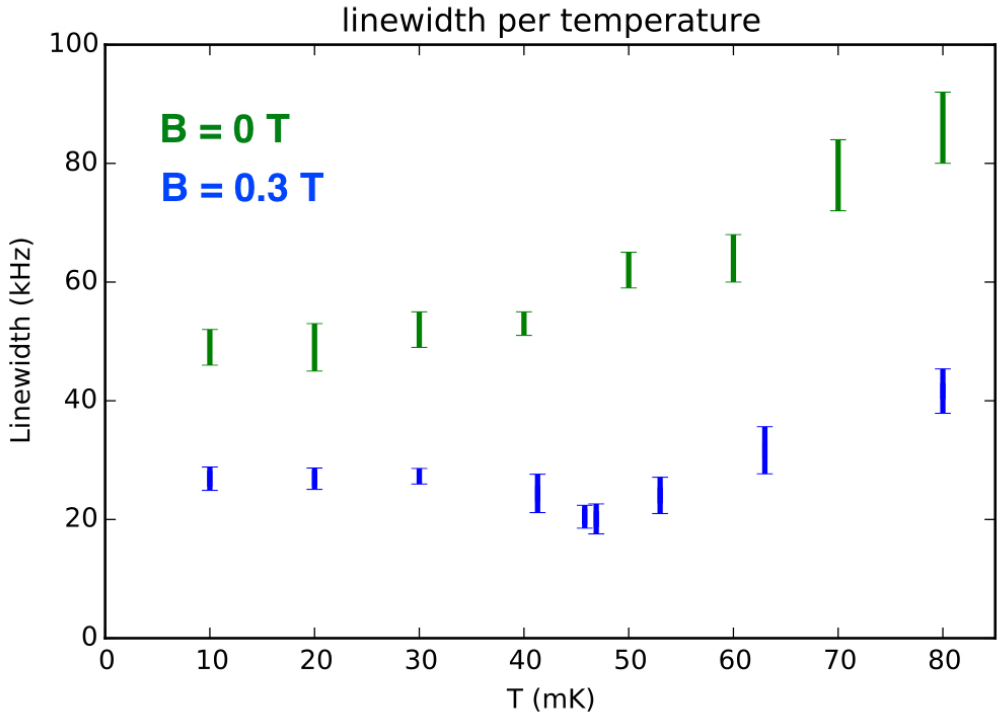

Figure 2.10: *The temperature-dependence of the homogeneous linewidth, for both $B = 0$ and $B = 0.3$ T.*

Here, the green markers represent the linewidth with zero magnetic field, while the blue markers are the data shown in figure 2.9. Roughly speaking, we see a reduction of maximally 30 kHz between the two. The linewidth for zero magnetic field shows the same decay for 52 mK $<$ T $<$ 80 mK as the linewidth for $B = 0.3$ T. While this local minimum around $T = 46$ mK is something which should be further investigated, we can state that an external magnetic field does decrease the homogeneous linewidth of the ytterbium in the ring resonator. In fact, at $T = 10$ mK, we see a reduction of approximately 22 kHz.

Chapter 3

Discussion

Figure 2.10 shows a very clear reduction in linewidth. The question now is what phenomenon can explain this behavior. In the background section, we identified two phenomena which could account for the low-temperature behaviour of sample. We found these phenomena in the literature.

- Dipole-dipole interactions. These are identified as being both possibly electric [14] and magnetic [6]. An electric dipole is of course stronger, but a magnetic dipole will be affected much more by magnetic field.
- Spin-elastic TS. This is the most popular explanation. We believe that these TS are a more plausible explanation than dipole-dipole interactions. Staudt and MacFarlane claim that the coupling of TS modes to rare earth elements gives the TS a magnetic character, making them susceptible to magnetic field [15], [28]. The main question here is: "Can TS modes couple to rare earth elements when we use isotopes without nuclear spin?"

Of crucial importance here, is to note that our ytterbium isotope has no nuclear spin. However, we see the same power law behaviour of the linewidth as a function of T as Staudt, and a reduction in linewidth as a result of an external magnetic field. So, an effect that relates an external magnetic field, to the linewidth decrease, via nuclear spin is excluded. Ytterbium does, however, have electronic spin ($s = 1/2$). The hypothesis we have -which would explain the homogeneous linewidth being reduced by a magnetic field- is TS-induced spectral diffusion. An intuitive picture of the way TS look inside the material, is depicted in figure 3.1. The energy landscape of these two states, is shown in figure 1.17.

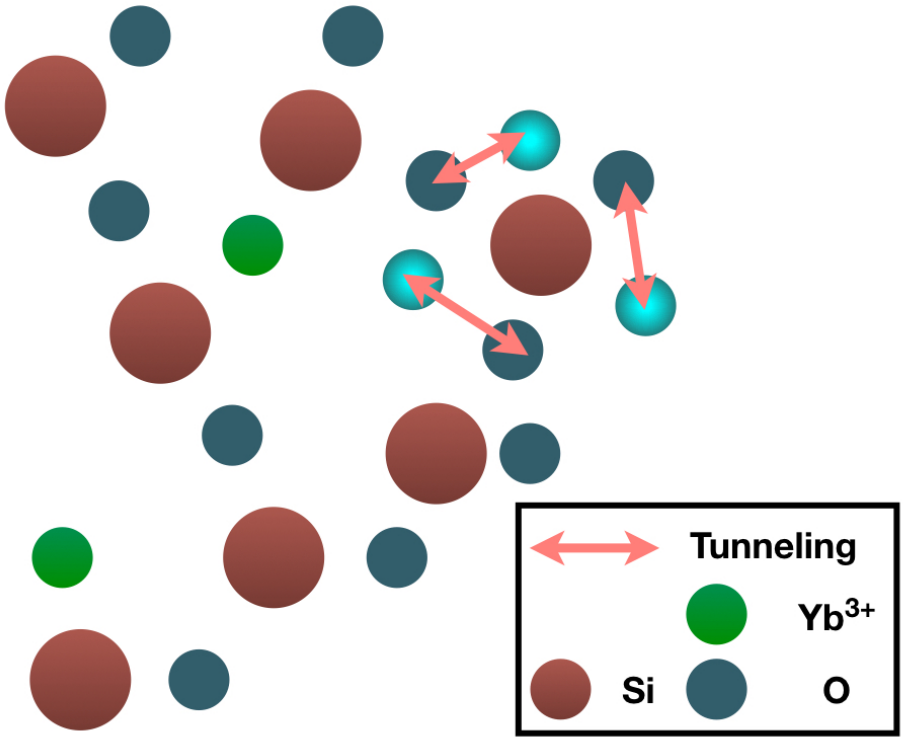

Figure 3.1: *The bright and dark blue circles are the tunneling system positions.*

Earlier, we discussed that the energy Yb^{3+} of ions can differ locally due to the amorphous structure of SiO_2. Atoms inside amorphous SiO_2 can slowly move inside the material. This process is known as spectral diffusion and is a mechanism for decoherence. Tunneling systems also allow atoms inside SiO_2 to move slightly over time. This way, it accounts for another type of spectral diffusion. As shown previously, a magnetic field decreases the tunneling probability. This way, the application of a magnetic field would also reduce the TS-induced spectral diffusion. This could be an explanation for the effect on the external magnetic field at such low temperatures.

Macfarlane et al. propose the following equation to describe the magnetic field,- and temperature-dependence of the homogeneous linewidth:

$$\Gamma_h(B,T) = \Gamma^0_{TLS}(T) + \Gamma^1_{TLS} exp(-g_{eff}\beta B/kT) \tag{3.1}$$

We tried to fit our data to this model. However, this formula could never fit our data correctly. There is no constant to which this formula will

converge when $T \to 0$. Macfarlane sees saturation for the magnetic field, but not for the temperature, like we do. Ultimately, the homogeneous linewidth has to saturate on the lifetime limit. This is the minimum value the homogeneous linewidth can take on, and is determined by T_1. We adjusted the model, so that it would fit our data. The resulting equation is:

$$\Gamma_h(B,T) = \Gamma^0_{TLS}T^2 + \Gamma^1_{TLS}exp(-g_{eff}\beta B/kT) + \Gamma_0 \tag{3.2}$$

We fit this equation for both $B = 0$ and $B = 0.3$ T. The results of which are shown in figure 3.2.

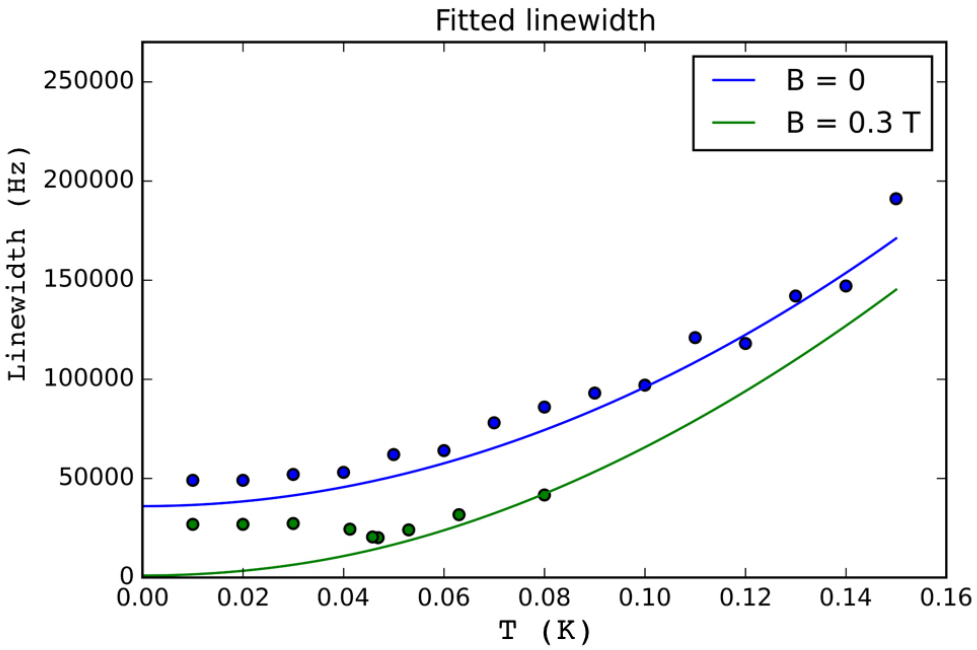

Figure 3.2: *Our data fitted to equation 3.2.*

The fit seems especially suitable for the $B = 0$ data. The $T^{1.3}$ term in the equation fits both datasets poorly. By changing the $T^{1.3}$ term to T^2, we got a much better fit for our data. The fit for $B = 0.3$ T, however, is not that good. For 0.045 K $< T <$ 0.08 K, the power law behaviour fits well. Below 0.04 K, the homogeneous linewidth seems to saturate. The value to which it saturates could be the lifetime limit. We know the equation for

the homogeneous linewidth to be:

$$\Gamma_h = \frac{1}{\pi T_1} + \frac{1}{2\pi T_2^*} = \frac{1}{4\pi T_2} \tag{3.3}$$

T_1 is constant, and T_2^* can be diminished by removing external perturbations. This means that, ultimately, T_2 is limited by T_1. This lifetime limit can be fairly high, meaning our system could have hit it already. For comparison, the telecom transition of Er^{3+} has a lifetime of 2 ms, which corresponds to a lifetime limit of approximately 150 Hz [21]. Our system has a lifetime of $T_1 = 0.31$ ms. Using equation 3.3, this gives us a lifetime limit of $\Gamma_{min} = 1.0$ kHz. For comparison, this is shown in 3.3.

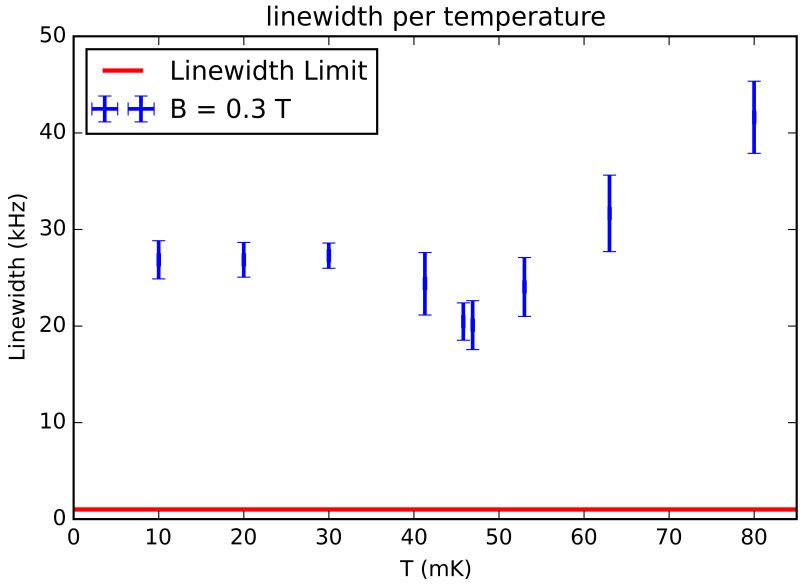

Figure 3.3: *The linewidth limit shown in comparison to our data.*

If we look at figure 3.3, this limit was certainly not hit. So, if the lifetime limit has not been reached yet, two other phenomena could account for this apparent saturation. Firstly, systematic error. Permanent magnets are well-known to change upon lowering the temperature. The fact that the magnetic field would decrease drastically between 80 mK and 10 mK seems unlikely [29]. To exclude this possibility, we would have to test the magnetic field strength at temperatures within this range to see the differences. The other explanation, would the existence of a hitherto undiscovered phenomenon. This phenomenon would have to explain why the behaviour of the linewidth changes below 30 mK.

So to conclude, we have researched the mechanisms determining the linewidth at millikelvin temperatures. We have compared our results to the current model. This did not match. To further explain the low-temperature behaviour of the homogeneous linewidth, additional research is required. Homogeneous linewidth measurements would have to be done at higher temperatures, both with, and without a magnetic field.

Chapter 4

Outlook

Through this research, we have explored what is needed to make a quantum memory. The question is now how the concept could be improved. First of all, other rare earth elements might be more sutiable. Erbium is a rare earth element, just as ytterbium is. Erbium is by far the most used rare earth element for experiments in optics. In the 1980's, it was mostly tested inside optical fibers. Nowadays, it is a prime candidate for an AFC quantum memory. Erbium has only 2 electrons less than ytterbium. Accordingly, its electronic configuration is: $[Er] = [Xe]4f^{12}6s^2$. Erbium in crystal/glass takes on the ionised form, namely: $[Er] = [Xe]4f^{11}$. So, erbium has 3 unpaired electron, allowing much more states than ytterbium. The two most important states are: $^4I_{15/2}$ and $^4I_{13/2}$. The transition between these two is very interesting in telecommunications [3].
A big difference between the two, is that erbium often has a nuclear spin, whilst our ytterbium isotope does not! At least 1 of the 6 stable erbium isotopes has s=$\frac{7}{2}$ [2]. This isotope does comprise more than 20 percent of all erbium. This difference could account for some phenomena which are apparently different in our experiment than in ones involving erbium. Also, the angular momentum of erbium is much higher ($^4I_{15/2}$ has L=6) than ytterbiums (L=3). So effects which involve coupling to such a momentum are potentially much stronger in erbium than in ytterbium. Erbium does have a very narrow linewidth.
Although the differences between ytterbium and erbium are large, the differences between glass and crystal might be even larger. Glass is a really difficult material to model. The amorphous structure makes it impossible to make reliable estimates with regard to it properties. Furthermore, the local differences can be very large. Ytterbium in one spot in the glass might have very different properties than in another spot. Furthermore,

various decoherence phenomena accompany glass due to its amorphous nature. The tunneling systems (TS) discussed earlier occur only in crystal defects or glass. The usage of crystal instead of glass as a host material for RE-doped ring resonators would have much longer coherence times as a result.
The new ring resonators as shown in 1.11 are also an advancement. Making ring resonators smaller also causes the mode volume to decrease. The Purcell factor scales like: $F \propto \frac{1}{V}$. If these ring resonators keep shrinking, the rate of spontaneous emission will increase drastically. This would ensure a much higher cavity response. In the future, this might even make ytterbium (or erbium) atoms individually addressable. Of course, to do so, the spectrum would have to be adjusted. This should be done by optically pumping ytterbium ions with unwanted frequencies to auxiliary levels. To conclude: quantum memory research is an exciting field. Very high precision is required, because one is dealing with single photons. Accordingly, low-temperature and decoherence phenomena have to be very well understood.

4.1 Acknowledgements

Thanks a lot: Wolfgang Löffler, Henk Snijders, Lino M. C. Pereira, Jared F. Bauters, Martijn J. R. Heck, Gesa Welker, André Vantomme, John E. Bowers, Michiel J. A. de Dood and Dirk Bouwmeester. Special thanks to Dapeng Ding, for setting up the experiments and guiding me through my research.

References

[1] Mikael Afzelius, Christoph Simon, Hugues de Riedmatten, and Nicolas Gisin. Multimode quantum memory based on atomic frequency combs. *Physical Review A*, 79(5):052329, may 2009.

[2] G. Audi, O. Bersillon, J. Blachot, and A.H. Wapstra. The N evaluation of nuclear and decay properties. *Nuclear Physics A*, 624(1):1–124, sep 1997.

[3] E Desurvire and J R Simpson. Evaluation of 4I15/2 and 4I13/2 Stark-level energies in erbium-doped aluminosilicate glass fibers. *Optics Letters*, 15(10):547–549, 1990.

[4] Dapeng Ding, Lino M C Pereira, Jared F Bauters, Martijn J R Heck, Gesa Welker, John E Bowers, Michiel J A De Dood, and Dirk Bouwmeester. Multi-dimensional Purcell effects in an ytterbium-doped ring resonator. pages 1–5.

[5] Feral Big Ten. Spring Water vs. Tap Liquid.

[6] D. L. Huber, M M Broer, and B. Golding. Low-Temperature Optical Dephasing of Rare-Earth Ions in Glass. *Physical Review Letters*, 52(25):2281–2284, 1984.

[7] P Jelger, K Seger, V Pasiskevicius, and F Laurell. Highly efficient temporally stable narrow linewidth cryogenically cooled Yb-fiber laser. *Optics express*, 17(10):8433–8438, 2009.

[8] Chun Jiang, Hua Liua, Qjji Zenga, Yun Wang, Junzhou Zhangb, and Fuxi Gan. 1Stark energy split characteristics of ytterbium ion in glasses. *Rare-Earth-Doped Materials and Devices IV*, 3942(2000):312–317, 2000.

[9] A.A. Kaplyanskii and R.M. Macfarlane. *SPECTROSCOPY OF SOLIDS CONTAINING RARE EARTH IONS*, volume 21. 187.

[10] T. Koubaa, M. Dammak, M. Kammoun, W. M. Jadwisienczak, H. J. Lozykowski, and A. Anders. Spectra and energy levels of Yb3+ in AIN. *Journal of Applied Physics*, 106(1):1–6, 2009.

[11] Stefan Kröl, Klaus Mølmer, and Mattias Nilsson. Quantum computing with rare-earth-ion doped crystals.

[12] Cyril Laplane, Pierre Jobez, Jean Etesse, Nuala Timoney, Nicolas Gisin, and Mikael Afzelius. Multiplexed on-demand storage of polarization qubits in a crystal. sep 2015.

[13] Lumerical. INTERCONNECT Ring Modulator Model.

[14] S. K. Lyo. Anomalous Optical Homogeneous Linewidths in Glasses. *Physical Review Letters*, 48(10):688–691, mar 1982.

[15] R. M. MacFarlane, Y. Sun, P. B. Sellin, and R. L. Cone. Optical decoherence in Er3+-doped silicate fiber: Evidence for coupled spin-elastic tunneling systems. *Physical Review Letters*, 96(3):3–6, 2006.

[16] Eric S. Maniloff, Felix R. Graf, Hansruedi Gygax, Stefan B. Altner, Stefan Bernet, Alois Renn, and Urs P. Wild. Power broadening of the spectral hole width in an optically thick sample. *Chemical Physics*, 193(1-2):173–180, 1995.

[17] W. B. Mims, K. Nassau, and J. D. McGee. Spectral Diffusion in Electron Resonance Lines. *Physical Review*, 123(6):2059–2069, sep 1961.

[18] Rüdiger Paschotta. Ytterbium-doped Gain Media.

[19] W. A. Phillips. Tunneling states in amorphous solids. *Journal of Low Temperature Physics*, 7(3-4):351–360, 1972.

[20] Frank Pobell. The 3 He – 4 He Dilution Refrigerator. *Matter and Methods at low Temperature*, pages 149–188, 2007.

[21] Francesco Priolo, Giorgia Franzò, Salvatore Coffa, and Alberto Carnera. Excitation and nonradiative deexcitation processes of Er 3 + in crystalline Si. *Physical Review B*, 57(8):4443–4455, feb 1998.

[22] E.M. Purcell. Spontaneous emission probabilities at radio frequencies. *Phys. Rev.*, 69:1946, 1946.

[23] V.A.G. Rivera, F.A. Ferri, and E. Marega. *Plasmonics - Principles and Applications*. InTech, oct 2012.

[24] H. N. Russell, A. G. Shenstone, and Louis A. Turner. Report on Notation for Atomic Spectra. *Physical Review*, 33(6):900–906, jun 1929.

[25] Mahmood Sabooni. *Efficient Quantum Memories Based on Spectral Engineering of Rare-Earth-Ion-Doped Solids*. PhD thesis, Lund, 2013.

[26] Albert Schliesser and Tobias J Kippenberg. Cavity optomechanics with whispering-gallery mode optical micro-resonators. (April), 2010.

[27] Y.R. Shen. *The Principles of Nonlinear Optics*. 2014.

[28] Matthias U. Staudt, Sara R. Hastings-Simon, Mikael Afzelius, Didier Jaccard, Wolfgang Tittel, and Nicolas Gisin. Investigations of optical coherence properties in an erbium-doped silicate fiber for quantum state storage. *Optics Communications*, 266(2):720–726, 2006.

[29] Stan Trout. Using Permanent Magnets at Low Temperatures.

[30] Wikipedia. Bloch sphere.

[31] Max Wolter. *Two-pulse dieletric polarisation echo experiments on the multicomponent glasses BK7 and HY-1*. PhD thesis, 2014.

[32] Changming Xia, Ying Han, GuiYao Zhou, and LanTian Hou. Preparation of Yb 3 + -doped Silica-based Glass for High Power Laser Applications.

[33] Manjin Zhong, Morgan P. Hedges, Rose L. Ahlefeldt, John G. Bartholomew, Sarah E. Beavan, Sven M. Wittig, Jevon J. Longdell, and Matthew J. Sellars. Optically addressable nuclear spins in a solid with a six-hour coherence time. *Nature*, 517(7533):177–180, 2015.